

Frequency-Tunable Microwave Field Detection in an Atomic Vapor Cell

Andrew Horsley* and Philipp Treutlein†

Department Physik, Universität Basel, CH-4056 Switzerland

(Dated: September 5, 2018)

We use an atomic vapor cell as a frequency tunable microwave field detector operating at frequencies from GHz to tens of GHz. We detect microwave magnetic fields from 2.3 GHz to 26.4 GHz, and measure the amplitude of the σ_+ component of an 18 GHz microwave field. Our proof-of-principle demonstration represents a four orders of magnitude extension of the frequency tunable range of atomic magnetometers from their previous dc to several MHz range. When integrated with a high-resolution microwave imaging system [1], this will allow for the complete reconstruction of the vector components of a microwave magnetic field and the relative phase between them. Potential applications include near-field characterisation of microwave circuitry and devices, and medical microwave sensing and imaging.

Atomic vapor cell magnetometers are among the most sensitive detectors for magnetic fields [2–4], and show promise in applications including gyroscopes [5], explosives detection [6], materials characterization [7–9], in MRI for both medical [10] and microfluidics applications [11], and for magnetic imaging of the human heart [12, 13] and brain [14–17]. Tunable atomic magnetometers have previously operated from dc to rf frequencies of a few MHz. In this letter, we demonstrate the principle of a continuously frequency tunable microwave magnetometer, capable of detecting magnetic fields from GHz to tens of GHz frequencies. This represents a four orders of magnitude extension of the atomic magnetometer frequency tunable range. Potential applications include near-field characterisation of microwave circuitry [1, 18–20], and medical microwave sensing and imaging [21–23], where high resolution, intrinsically calibrated atomic sensors could replace bulky and field-perturbing antennas.

At the fixed microwave frequency of 6.8 GHz, we have previously used atoms to produce polarisation-resolved images of microwave magnetic near-field distributions [1, 24–27]. We have achieved $50 \times 50 \times 140 \mu\text{m}^3$ spatial resolution and $1 \mu\text{T}/\text{Hz}^{-1/2}$ sensitivity, observing good agreement between the measured fields and simulations for simple test structures [1]. (Atom-like) NV centres have recently been used for nanoscale near-field detection [28] and imaging [29], and microwave *electric* field imaging has also been demonstrated at discrete frequencies using Rydberg atoms [30–33]. To-date, however, there has been no atomic sensor available for the detection of fields at arbitrary microwave frequencies, as required for most applications.

Our frequency-tunable sensing scheme is able to operate in either of two modes: to detect microwaves of unknown frequency (i.e. as a microwave spectrum analyser); or to accurately measure the amplitudes of microwave magnetic fields (B_{mw}) of known frequency. In this letter, we focus on the latter, measuring B_{mw}

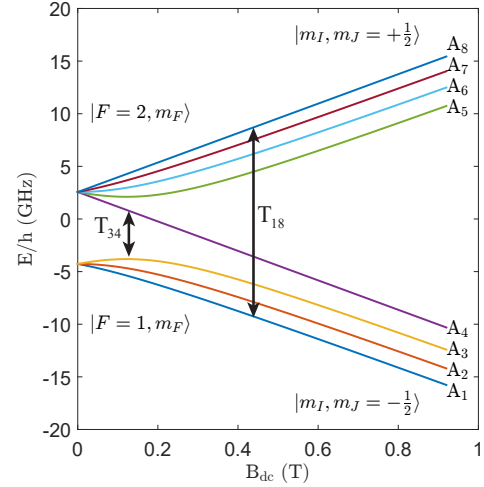


FIG. 1. (Color online) Energy splitting of the ^{87}Rb hyperfine ground state levels as a function of applied dc magnetic field. Arrows indicate the hyperfine transitions used in this work.

through coherent Rabi oscillations driven by the microwave on atomic hyperfine transitions [24, 25]. The atomic transitions are sensitive to a narrow microwave frequency band, and we use a dc magnetic field (B_{dc}) to tune the transition frequency to the desired value. This is conceptually similar to rf magnetometry, where a dc magnetic field is used to tune the Zeeman splitting of adjacent m_F states [3]. However, much larger dc fields are required for microwave frequencies, bringing us into the hyperfine Paschen-Back regime. Moreover, since our technique is based on measurements of frequency rather than amplitude, it is intrinsically calibrated and less sensitive to environmental noise. In this letter, we work with the ^{87}Rb hyperfine ground states, however our technique is applicable to any microwave magnetic dipole transition with optical read-out of one of the states, such as other alkali atoms and NV centres.

Figure 1 shows the splitting of the ^{87}Rb $5S_{1/2}$ ground state in an applied dc magnetic field, calculated using the Breit-Rabi formula [34]. We label the 8 hyperfine states $A_1 \rightarrow A_8$, in order of increasing energy. At $B_{\text{dc}} = 0$,

* andrew.horsley@unibas.ch

† philipp.treutlein@unibas.ch

the states are grouped according to the $|F, m_F\rangle$ basis defined by the atomic Hamiltonian, and split by 6.8 GHz. As B_{dc} is increased, the hyperfine states move towards the $|I, m_I, J, m_J\rangle$ basis defined by the dc field. This is accompanied by a corresponding shift in transition frequencies and coupling strengths between the hyperfine states. An applied microwave field will drive Rabi oscillations on a given transition that has been tuned to resonance. The amplitude of the microwave vector component B_γ is given by the measured Rabi oscillation frequency, Ω_R , the transition matrix element, and well-known fundamental constants. For a microwave resonant with transition T_{if} , we have

$$B_\gamma = |\alpha_{if}| \frac{\hbar}{\mu_B} |\Omega_R|, \quad (1)$$

where $\gamma = -, \pi, +$ is the polarisation of the transition, and

$$\alpha_{if} \equiv \frac{1}{2\langle A_f | J_\gamma | A_i \rangle}. \quad (2)$$

The coupling factor α_{if} is a function of the applied dc magnetic field. As B_{dc} increases, $\alpha \rightarrow 1$ for the σ_+ polarised transitions, and $\alpha \rightarrow 0$ for the σ_- and π transitions. For ^{87}Rb , we can find σ_- (π) transitions where $|\alpha| > 0.15$ for microwave frequencies within the range 2.2–9.1 GHz (5.9–22.8 GHz) [35]. Strong σ_+ transitions are available for all frequencies. Previous B_{mw} reconstruction schemes have relied on the presence of strong π transitions [1]. However, it is possible to completely reconstruct the vector components of the microwave magnetic field amplitude, and the relative phases between them, using only σ_+ transitions [35]. The reconstruction then requires measurements of B_+ with the dc magnetic field both parallel and anti-parallel to each of the lab-frame x , y , and z axes. In this letter, we address two microwave transitions: the σ_+ polarised T_{18} transition, and the σ_- polarised T_{34} transition.

We use a 2 mm thick, microfabricated vapor cell (Fig. 2(a)), filled with natural Rb and 63 mbar of N_2 buffer gas [26, 36]. Doppler and collisional broadening result in an optical linewidth of 1.5 GHz. We use a 780 nm laser, linearly polarised along B_{dc} , for both optical pumping and probing. A water-cooled solenoid [37] provides dc magnetic fields up to 0.8 T (Fig. 2.(b)). We heat the vapor cell using a 2 W laser at 1500 nm [35, 38], and obtain the cell temperature by fitting optical absorption spectra (taken at $B_{dc} = 0$) with the model described in Ref. [39].

We can detect microwaves over a broad range of frequencies. Figure 3(a) shows experimentally obtained double-resonance (DR) peaks for microwaves spanning frequencies from 2.3 GHz to 26.4 GHz. The laser beam is applied continuously, and its frequency is tuned to resonance with one of the hyperfine states. This partially depopulates the state through optical pumping. Through the transmission of the laser onto a photodiode, we monitor the change in optical density (OD_{mw}) as we sweep

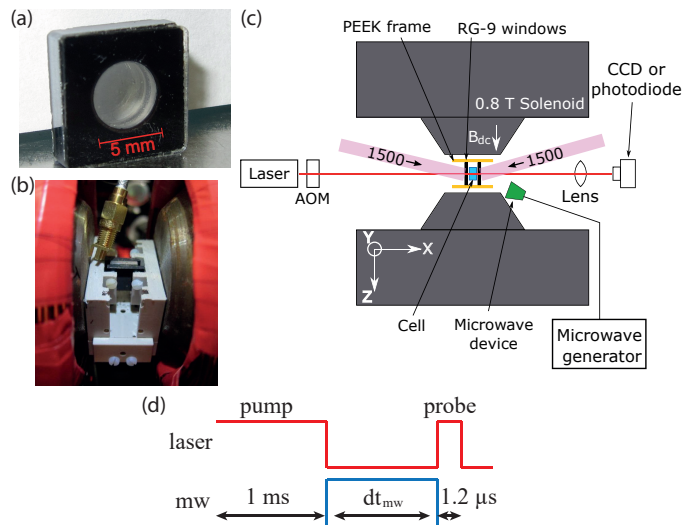


FIG. 2. (Color online) (a) The vapor cell; (b) the experiment setup, showing the vapor cell sandwiched between two RG-9 glass pieces and mounted on the PEEK frame inside the solenoid. The gold microwave output coupler can be seen above the cell; (c) schematic of the experiment setup; (d) the Rabi sequence used to obtain microwave amplitudes.

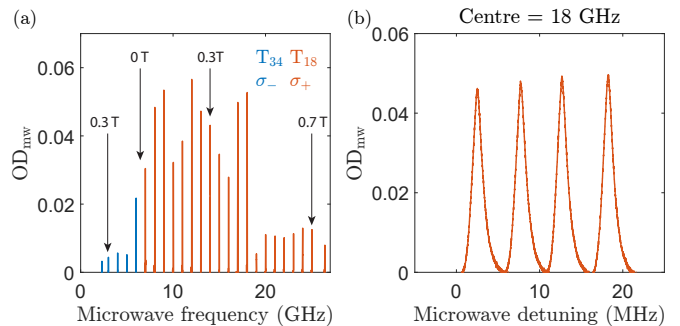


FIG. 3. (Color online) Detection of microwave signals at arbitrary frequencies. (a) DR detection of frequencies ranging from 2.3 GHz to 26.4 GHz. Each peak corresponds to a single experimental run taken using a different B_{dc} . The data was taken on both the T_{34} (blue) and T_{18} (red) transitions, and shows the change in optical density induced by the microwave. Labels in black indicate relevant B_{dc} strengths. (b) DR peaks for frequencies near 18 GHz, showing fine-tuning of the detection frequency by adjusting B_{dc} .

the frequency of an applied microwave field. Whenever the microwave frequency crosses a hyperfine transition coupling to the optically pumped state, we see a peak in OD_{mw} , corresponding to repopulation of the state. Each peak in Fig. 3 represents a separate measurement, with B_{dc} changed between measurements. Peaks in the range 7–26.4 GHz (red) were measured on the σ_+ T_{18} transition, whilst peaks in the range 2.3–6 GHz (blue) were measured on the σ_- T_{34} transition. The laser beam probed the approximate spatial centre of the dc magnetic field (see Fig. 4(b)), with inhomogeneities in the dc field

resulting in a 1 MHz (FWHM) DR linewidth. The peak area is proportional to Ω_R , however it is also sensitive to fluctuations in the laser intensity and cell temperature, and calibration with a known field is required to extract Ω_R . For fixed conditions (not shown), we observe the expected linear scaling of the peak area with the square-root of the microwave power. The lower limit on microwave frequency in Fig. 3(a) was imposed by the asymptotic behaviour of the T_{34} transition frequency at high B_{dc} [35]. Other transitions (e.g. T_{45}) are available with frequencies down to dc, in which case the lower detection limit will be given by the optical distinguishability of neighbouring hyperfine states, in general on the order of the 0.5 GHz Doppler broadening in a cell without buffer gas. The upper frequency limit is given only by technical limitations, e.g. the available B_{dc} strength, or in our case the microwave frequency generator.

The dc magnetic field provides fine control over the microwave detection frequency, as shown in Fig. 3(b). Each DR peak represents a single measurement on the T_{18} transition, with the zero of the horizontal axis corresponding to a microwave frequency of 18 GHz. By scanning B_{dc} , such DR measurements could be used in a spectrum analyser mode, to search for microwave fields of unknown frequency.

For an accurate measure of the B_{mw} amplitude, we need to measure the Rabi frequency directly. We demonstrate this by measuring the σ_+ amplitude of an 18 GHz microwave. The observed oscillations are a function of both microwave amplitude ($\propto \Omega_R$) and detuning from resonance (Δ), with a frequency $\Omega = \sqrt{\Omega_R^2 + \Delta^2}$. In general, it is simple to directly measure the detuning, e.g. from the peak of a DR scan. We use a relatively thick cell in our proof-of-principle setup, however, and must account for a non-negligible B_{dc} inhomogeneity along the x axis, which the laser integrates over as it passes through the cell. Our experiment ‘Rabi’ sequence, shown schematically in Fig. 2(d), begins with an optical pumping pulse to depopulate the A_1 state. A microwave pulse of duration dt_{mw} then drives Rabi oscillations between the A_1 and A_8 states, and we detect the repopulation of the A_1 state (i.e. OD_{mw}) with a $1.2 \mu s$ probe laser pulse. We repeat this sequence, scanning either the frequency (Fig. 4(c)) or duration (Fig. 4(d)) of the microwave pulse. The frequency domain scan primarily constrains B_{dc} (Fig. 4(b)), and we extract the B_{mw} amplitude by simultaneously fitting the two scans [35]. In future setups, the frequency domain scan will be unnecessary.

We used the T_{18} transition for sensing, with the frequency of the laser tuned to address the A_1 level. A solenoid field of $B_{dc} \approx 0.44$ T tuned the T_{18} transition of atoms in the B_{dc} field centre to resonance with the applied 18 GHz microwave. At this dc field, the A_1 level is optically well-resolved [40], and almost all of the measured optical density of $OD = 2.1$ was due to atoms in the A_1 state. The frequency domain scan was performed around 18.003 GHz with a fixed microwave pulse dura-

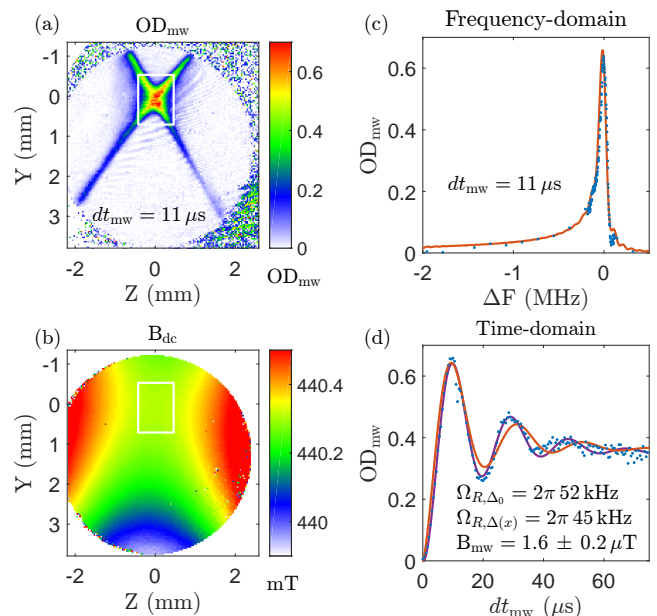


FIG. 4. (Color online) Measuring an 18.003 GHz microwave field amplitude. Experimentally obtained images of (a) OD_{mw} for a microwave pulse resonant with the T_{18} transition in the B_{dc} field centre; (b) map of the local B_{dc} field extracted from measurements as in (a). The circular field of view is given by the cell walls, and the white boxes indicate the region appropriate for microwave sensing; (c+d) scans in the frequency and time domains, for the pixel at ($z = 2.29$ mm, $y = 1.32$ mm). Fits are shown assuming a constant microwave detuning along the x axis (purple, time domain only, Ω_{R,Δ_0}), and allowing for an inhomogeneous detuning (red, simultaneous fit to time and frequency domain data, $\Omega_{R,\Delta(x)}$).

tion of $dt_{mw} = 11 \mu s$, corresponding roughly to a π pulse in the centre of the B_{dc} field, while the time domain scan was performed with a fixed frequency of 18.003 GHz.

We are working towards frequency tunable microwave imaging, and therefore use a CCD camera and the technique of absorption imaging for detection [1, 40, 41]. The laser illuminates the entire cell, and we obtain images of OD_{mw} (Fig. 4(a)). Due to inhomogeneities in the B_{dc} field, we only present microwave detection for a single pixel near the B_{dc} centre. If only single-channel sensing is required, real-time monitoring of the Rabi oscillations should also be possible using a photodiode and an off-resonant probe laser. The atomic response traced a contour line of the B_{dc} field in the cell, as illustrated in Fig. 4(a), which shows an image of OD_{mw} for an $11 \mu s$ long 18.003 GHz microwave pulse. Scanning the microwave frequency (Fig. 4(c)), we could quickly estimate the local T_{18} transition frequency from the peak in OD_{mw} . Using the Breit-Rabi formula, this transition frequency yielded an image of the applied B_{dc} , shown in Fig. 4(b). We see that the solenoid field is saddle-shaped, homogeneous to better than 10^{-3} , but nonetheless varying by several Gauss over the cell. The plane of the image is slightly offset from the $x = 0$ centre of the solenoid

field.

The simultaneous fit of the Fig. 4(c+d) frequency and time domain data, described in detail in the supplementary material, yielded a Rabi frequency of $\Omega_{R,\Delta(x)} = 2\pi 45$ kHz, corresponding to $B_{mw} = 1.6 \mu\text{T}$. The shape of the frequency scan data in Fig. 4(c) is primarily determined by the variation in B_{dc} along the x axis, and is well-matched by the fit. The peak corresponds to atoms around the B_{dc} centre, where the field is relatively flat, while the long tail is due to the drop-off of B_{dc} away from the centre. The time domain fit in Fig. 4(d) underestimates the oscillation frequency, due to constraints imposed by the simultaneous fitting of time and frequency domain data with our relatively simple model. In fact, we find much better agreement with the time domain data if we simply assume a constant $\Delta_0 = -4$ kHz, given by the frequency domain peak position, and fit to the time domain data only. This is shown by the purple line in Fig. 4(d), and we obtain $\Omega_{R,\Delta_0} = 2\pi 52$ kHz, corresponding to $B_{mw} = 1.8 \mu\text{T}$. By neglecting the range of larger detunings along the x axis, this value serves as an upper bound on B_{mw} . We can therefore estimate a B_{mw} accuracy of 10% in our current proof-of-principle setup. We emphasise that in a high resolution setup using a thinner vapor cell [1], the image analysis will be much simpler, with B_{mw} directly extracted from time domain data and accuracy on the 10^{-3} level.

In conclusion, we have presented a proof-of-principle demonstration of microwave magnetic field detection for microwaves of any frequency, obtaining the amplitude of the σ_+ component of an 18 GHz microwave field, and detecting magnetic fields at frequencies from 2.3 GHz to 26.4 GHz. Magnetic field detection of frequencies up to 50 GHz should be achievable with room-temperature iron-bore solenoids (which can operate to ~ 1.6 T), and given sufficient dc field homogeneity, it may be possible to detect fields up to 1 THz using the strongest available superconducting solenoids (>35 T). It would be interesting to explore the frequency tunability presented here

with other detection techniques, such as Faraday rotation or EIT, and with other systems, such as NV centres [29].

Our frequency tunable detection provides an essential step towards an atom-based characterisation tool for microwave devices operating at any frequency. To realise this in practical form, the frequency tunability demonstrated in this letter should now be integrated with a high resolution imaging setup [1]. We note, however, that for some devices, such as circulators, the large applied B_{dc} fields may significantly perturb the device operation. High spatial resolution, provided by a thin vapor cell, will have the added benefit of significantly reducing our sensitivity to B_{dc} inhomogeneities. For a $200 \mu\text{m}$ thick cell operating in the B_{dc} field shown in Fig 4(b), B_{dc} variation along the x axis should be negligible, on the order of $2\pi \times 1$ kHz. The transverse variation over a $50 \times 50 \mu\text{m}^2$ pixel at the B_{dc} centre would be $2\pi \times 0.2$ kHz, increasing to $2\pi \times 80$ kHz at a distance 1 mm either side of the centre. This is entirely acceptable compared to the tens to hundreds of kHz Rabi frequencies observed in Ref. [1]. Moreover, the B_{dc} inhomogeneity could also be reduced by using shimming coils. We expect the sensitivity to be slightly better than for the fixed-frequency imaging reported in Ref. [1], due to the suppression of Rb spin-exchange relaxation in large B_{dc} fields [42]. The integrated setup could be miniaturised by replacing the bulky solenoid with permanent rare-earth magnets, with B_{dc} adjusted through the magnet separation [43, 44].

ACKNOWLEDGMENTS

This work was supported by the Swiss National Science Foundation (SNFS). We thank G. Mileti, C. Affolderbach, and Y. Pétremand for providing the vapor cell, and the group of P. Maletinsky for the loan of microwave circuitry. We also thank M. Belloni for interesting discussions, and C. Affolderbach for careful reading of the manuscript.

-
- [1] A. Horsley, G.-X. Du, and P. Treutlein, *New J. Phys.* **17**, 112002 (2015).
 - [2] D. Budker and M. Romalis, *Nature Physics* **3**, 227 (2007).
 - [3] I. M. Savukov, S. J. Seltzer, M. V. Romalis, and K. L. Sauer, *Phys. Rev. Lett.* **95**, 063004 (2005).
 - [4] D. Sheng, S. Li, N. Dural, and M. V. Romalis, *Phys. Rev. Lett.* **110**, 160802 (2013).
 - [5] E. A. Donley, J. L. Long, T. C. Liebisch, E. R. Hodby, T. A. Fisher, and J. Kitching, *Phys. Rev. A* **79**, 013420 (2009).
 - [6] S.-K. Lee, K. L. Sauer, S. J. Seltzer, O. Alem, and M. V. Romalis, *Appl. Phys. Lett.* **89**, 214106 (2006).
 - [7] M. V. Romalis and H. B. Dang, *Mater. Today* **14**, 258 (2011).
 - [8] C. Deans, L. Marmugi, S. Hussain, and F. Renzoni, *Appl. Phys. Lett.* **108**, 103503 (2016).
 - [9] A. Wickenbrock, N. Leefer, J. W. Blanchard, and D. Budker, (2016), arXiv:1603.05067.
 - [10] I. Savukov and T. Karaulanov, *J. of Mag. Res.* **231**, 39 (2013).
 - [11] S. Xu, C. W. Crawford, S. Rochester, V. Yashchuk, D. Budker, and A. Pines, *Phys. Rev. A* **78**, 013404 (2008).
 - [12] G. Bison, N. Castagna, A. Hofer, P. Knowles, J.-L. Schenker, M. Kasprzak, H. Saudan, and A. Weis, *Appl. Phys. Lett.* **95**, 173701 (2009).
 - [13] O. Alem, T. H. Sander, R. Mhaskar, J. LeBlanc, H. Eswaran, U. Steinhoff, Y. Okada, J. Kitching, L. Trahms, and S. Knappe, *Phys. Med. Biol.* **60**, 4797 (2015).
 - [14] I. Savukov and T. Karaulanov, *Appl. Phys. Lett.* **103**, 43703 (2013).
 - [15] C. N. Johnson, P. D. D. Schwindt, and M. Weisend, *Phys. Med. Biol.* **58**, 6065 (2013).

- [16] R. Wyllie, M. Kauer, R. T. Wakai, and T. G. Walker, *Opt. Lett.* **37**, 2247 (2012).
- [17] V. K. Shah and R. T. Wakai, *Phys. Med. Biol.* **58**, 8153 (2013).
- [18] S. Sayil, D. J. Kerns, and S. Kerns, *IEEE Trans. Instrum. Meas.* **54**, 2082 (2005).
- [19] T. Dubois, S. Jarrix, A. Penarier, P. Nouvel, D. Gasquet, L. Chusseau, and B. Azais, *IEEE Trans. Instrum. Meas.* **57**, 2398 (2008).
- [20] G. M. Sardi, A. Lucibello, M. Kasper, G. Gramse, E. Proietti, F. Kienberger, and R. Marcelli, *Appl. Phys. Lett.* **107**, 033107 (2015).
- [21] E. C. Fear, S. C. Hagness, P. M. Meaney, M. Okoniewski, and M. A. Stuchly, *Microwave Magazine*, *IEEE* **3**, 48 (2002).
- [22] N. Nikolova, *IEEE Microwave Magazine* **12**, 78 (2011).
- [23] R. Chandra, H. Zhou, I. Balasingham, and R. M. Narayanan, *IEEE Trans. Biomed. Eng.* **62**, 1667 (2015).
- [24] P. Böhi, M. F. Riedel, T. W. Hänsch, and P. Treutlein, *Appl. Phys. Lett.* **97**, 051101 (2010).
- [25] P. Böhi and P. Treutlein, *Appl. Phys. Lett.* **101**, 181107 (2012).
- [26] A. Horsley, G.-X. Du, M. Pellaton, C. Affolderbach, G. Miletì, and P. Treutlein, *Phys. Rev. A* **88**, 063407 (2013).
- [27] C. Affolderbach, G.-X. Du, T. Bandi, A. Horsley, P. Treutlein, and G. Miletì, *IEEE Trans. Instrum. Meas.* **64**, 3629 (2015).
- [28] P. Wang, Z. Yuan, P. Huang, X. Rong, M. Wang, X. Xu, C. Duan, C. Ju, F. Shi, and J. Du, *Nat. Commun.* **6**, 6631 (2015).
- [29] P. Appel, M. Ganzhorn, E. Neu, and P. Maletinsky, *New J. Phys.* **17**, 112001 (2015).
- [30] J. A. Sedlacek, A. Schwettmann, H. Kübler, R. Löw, T. Pfau, and J. P. Shaffer, *Nat. Phys.* **8**, 819 (2012).
- [31] C. Holloway and J. Gordon, *Appl. Phys. Lett.* **104**, 244102 (2014).
- [32] H. Q. Fan, S. Kumar, R. Daschner, H. Kübler, and J. P. Shaffer, *Opt. Lett.* **39**, 3030 (2014).
- [33] H. Fan, S. Kumar, J. Sedlacek, H. Kübler, S. Karimkashi, and J. P. Shaffer, *J. Phys. B* **48**, 202001 (2015).
- [34] D. A. Steck, “Rubidium 87 D Line Data,” available online at <http://steck.us/alkalidata> (revision 2.1.4, 23 December 2010).
- [35] See supplementary material.
- [36] M. Pellaton, C. Affolderbach, Y. Pétremand, N. de Rooij, and G. Miletì, *Physica Scripta* **T149**, 014013 (2012).
- [37] Brukner, B-E 10 solenoid with B-MN C4 power supply, built in 1974.
- [38] R. Mhaskar, S. Knappe, and J. Kitching, *Appl. Phys. Lett.* **101**, 5 (2012).
- [39] M. A. Zentile, J. Keaveney, L. Weller, D. J. Whiting, C. S. Adams, and I. G. Hughes, *Comput. Phys. Commun.* **189**, 162 (2015).
- [40] A. Horsley, PhD Thesis, Department of Physics, University of Basel, Switzerland (2015).
- [41] A. Horsley, G.-X. Du, M. Pellaton, C. Affolderbach, G. Miletì, and P. Treutlein, *Proc. 2013 Joint IEEE-UFFC, EFTF and PFM Symposium*, 575 (2013).
- [42] S. Kadlecek, T. Walker, D. K. Walter, C. Erickson, and W. Happer, *Physical Review A* **63**, 052717 (2001).
- [43] L. Weller, K. S. Kleinbach, M. A. Zentile, S. Knappe, I. G. Hughes, and C. S. Adams, *Opt. Lett.* **37**, 2 (2012).
- [44] M. A. Zentile, R. Andrews, L. Weller, S. Knappe, C. S. Adams, and I. G. Hughes, *J. Phys. B* **47**, 075005 (2014).

Frequency-Tunable Microwave Field Detection in an Atomic Vapor Cell: Supplementary Information

Andrew Horsley* and Philipp Treutlein†
Departement Physik, Universität Basel, CH-4056 Switzerland
 (Dated: September 5, 2018)

I. MICROWAVE AMPLITUDE EXTRACTION

To account for the x axis variation in B_{dc} that the laser integrates over as it passes through the vapor cell, we take data in both the time and frequency domains, and perform a simultaneous fit to both data sets. Broadly speaking, the frequency domain data constrains the B_{dc} variation, and the time domain data gives us the microwave Rabi frequency. In future high resolution setups, the vapor cell will be sufficiently thin that B_{dc} variation through the cell will be negligible, rendering this frequency domain scan and simultaneous fitting process unnecessary. For our current proof-of-principle setup, we fit the data using

$$\text{OD}_{\text{mw}} = \int dx \left[A \frac{\Omega_R^2}{\Omega_R^2 + \Delta(x)^2} \sin^2 \left(\frac{1}{2} \sqrt{\Omega_R^2 + \Delta(x)^2} dt_{\text{mw}} \right) \right. \\ \left. \times \exp(-dt_{\text{mw}}/\tau_2) + B \frac{\Omega_R^2}{\Omega_R^2 + \Delta(x)^2} \left(1 - \exp(-dt_{\text{mw}}/\tau_1) \right) \right], \quad (\text{S1})$$

where A , B , Ω_R , $\Delta(x)$, τ_1 , and τ_2 are fit parameters. The first term describes Rabi oscillations with a coherence time τ_2 . The second term is phenomenological, accounting for the diffusion of atoms from neighbouring regions of the cell, with a time constant τ_1 . We neglect variation in Ω_R along the x axis, as there was little variation in distance from the microwave source for a given y - z position through the cell. We include the B_{dc} inhomogeneity along the x axis by using $\Delta(x) = \delta\omega_0 - \delta\omega_2(x - x_0)^2 - \delta\omega_4(x - x_0)^4$, where x_0 is the x axis centre of the B_{dc} field. This form is derived from the measured B_{dc} variation along the y axis (Fig. 4(b) in the main text), justified by the cylindrical symmetry of the solenoid.

For the pixel at ($z = 0$ mm, $y = 0$ mm), shown in Figs. 4(c+d) of the main text, the fit parameters are $A = 2.1$, $B = 0.88$, $\tau_1 = 15 \mu\text{s}$, $\tau_2 = 18 \mu\text{s}$, $x_0 = 0.55$ mm, $\delta\omega_0 = 2\pi 4.4$ kHz, $\delta\omega_2 = 2\pi 260$ kHz/mm², $\delta\omega_4 = 2\pi 250$ kHz/mm⁴, and $\Omega_{R,\Delta(x)} = 2\pi 45$ kHz. The coupling constant between the Rabi frequency and microwave amplitude is essentially a constant value of $\alpha_{18} = 0.492$ over the cell. The extracted Rabi frequency of $\Omega_{R,\Delta(x)} = 2\pi 45$ kHz thus corresponds to $B_{\text{mw}} = 1.6 \mu\text{T}$. The coherence time is around 10% of

the optically pumped population lifetime (T_1), with the dominant dephasing mechanism caused by fluctuations in Zeeman shift due to atomic motion through the B_{dc} inhomogeneities.

II. FURTHER B_{mw} DETECTION DETAILS

Due to the large dc magnetic fields and spatial constraints imposed by the solenoid, we avoided using resistive heaters to control the cell temperature. Instead, the cell was placed between two 2 mm thick pieces of RG9 glass (strongly absorptive at 1500 nm, with better than 90% transmission at 780 nm), and we heated the glass using a 2 W laser at the wavelength of 1500 nm. The direct heating of the cell windows ensures that there is minimal build-up of Rb on the windows, and the localised cell heating is advantageous for detecting microwave fields produced by temperature-sensitive devices. We were able to operate at relatively high temperatures with minimal reduction in T_1 lifetime, due to the suppression of Rb-Rb spin exchange relaxation in large dc magnetic fields [S1].

For the data presented in Fig. 3 of the main text, the 780 nm laser intensity was 5 mW/cm² and the beam diameter was 0.6 mm. The data in Fig. 3(b) was taken at a cell temperature of 99°C.

For the data presented in Fig. 4 of the main text, the 780 nm laser beam was expanded to cover the entire vapor cell, with an intensity of 120 mW/cm² averaged over the central 3 mm. The cell temperature was 115°C. We repeated the frequency and time domain scans 3 and 5 times, respectively. Fitting was performed on the averaged data, however before further analysis, we binned the CCD pixels into 3×3 blocks to create $35.5 \times 35.5 \mu\text{m}^2$ image pixels. This reduced the computational intensity of the data analysis, with minimal reduction in image quality, as the image pixel size was still significantly smaller than the 0.11 mm diffusion distance of atoms during their coherence lifetime (for $P_{\text{fill}} = 63$ mbar N₂, $T_{\text{fill}} = 80^\circ\text{C}$, $T_{\text{cell}} = 115^\circ\text{C}$, we have $D = 3.4$ cm²/s. Using $\Delta x = \sqrt{2D dt}$ and $dt = 18 \mu\text{s}$, $\Delta x = 0.11$ mm). The frequency domain data was taken less than 5 minutes after the time domain data, allowing us to minimise the effects of drifts in the B_{dc} field, which occurred with a timescale of several minutes to tens of minutes. These drifts also complicated the practical implementation of shimming fields to homogenise the solenoid field. However, we note that no attempt was made to actively stabilise the solenoid, and that solenoid stability and homogeneity have likely advanced in the decades since the

* andrew.horsley@unibas.ch

† philipp.treutlein@unibas.ch

solenoid was purchased in 1974.

The metallic poles of the magnet will impose boundary conditions on the microwaves. This may be a significant perturbation for the detection of far-field microwaves, as the 26 mm separation of our solenoid poles is comparable to microwave wavelengths. However, we do not expect the poles to be a problem in the detection of microwave near-fields hundreds of micrometers to a few millimeters above a source, which would be the operation mode for microwave device characterisation as in Ref. [S2].

Regarding the variation of the B_{dc} field along the x axis, we can define three regions: a ‘good’ central region, where the B_{dc} field is relatively flat and atoms are near resonance with the microwave; two ‘bad’ middle regions, in front of and behind the ‘good’ region, where the detuning is small enough for the atoms to still undergo Rabi oscillations, but at a significantly different oscillation frequency to the ‘good’ region, thus acting to wash out the ‘good’ signal; and two ‘neutral’ outer regions, where atoms are so far detuned from the microwave that they do not interact. We minimised the ‘bad’ effects by placing the vapor cell mount on a translation stage, and adjusting the cell position to minimise the double-resonance linewidth. In doing so, we aligned the front of the cell with the edge of the ‘good’ region, meaning that the atoms only saw one ‘bad’ region, and an extended ‘neutral’ region. The sensing region for B_{mw} was primarily in the ‘good’ region, thinner than the full 2 mm thickness of the cell.

III. HYPERFINE TRANSITIONS IN AN ARBITRARY DC MAGNETIC FIELD

The Hamiltonian for the hyperfine splitting of an atom in an external dc magnetic field $\mathbf{B}_{dc} = B_z \hat{z}$ is

$$H = H_{\text{hfs}} + H_Z = A_{\text{hfs}} \mathbf{I} \cdot \mathbf{J} + \mu_B (g_I I_z + g_J J_z) B_z, \quad (\text{S2})$$

where H_{hfs} is the hyperfine coupling Hamiltonian, H_Z is the Zeeman Hamiltonian, \mathbf{I} and \mathbf{J} are the atomic nuclear and electronic spin, respectively, g_I and g_J are the corresponding g -factors, and A_{hfs} is the hyperfine coupling constant [S3]. The energies of each hyperfine level can be obtained numerically from the eigenvalues of H , or analytically by using the Breit-Rabi formula. This is shown as a function of dc magnetic field for the ^{87}Rb $5S_{1/2}$ hyperfine levels in Fig. 1 of the main text. The levels are labelled $A_1 \rightarrow A_8$, in order of increasing energy ($E_1 < E_2 \dots < E_8$). The resulting hyperfine transition frequencies are shown in Fig. S1. Transitions between levels A_i and A_f are labelled T_{if} , with energies $E_{if} = E_f - E_i$. The σ_+ transitions are shown in red, π transitions in green, and σ_- transitions are shown in blue.

The H_Z term in Eq. (S2) means that as the magnetic field is scanned, the eigenfunctions of the Hamiltonian must change. It is therefore best to describe the hyperfine levels in some field-independent basis, for which the $|I, m_I, J, m_J\rangle$ basis is a convenient choice. As

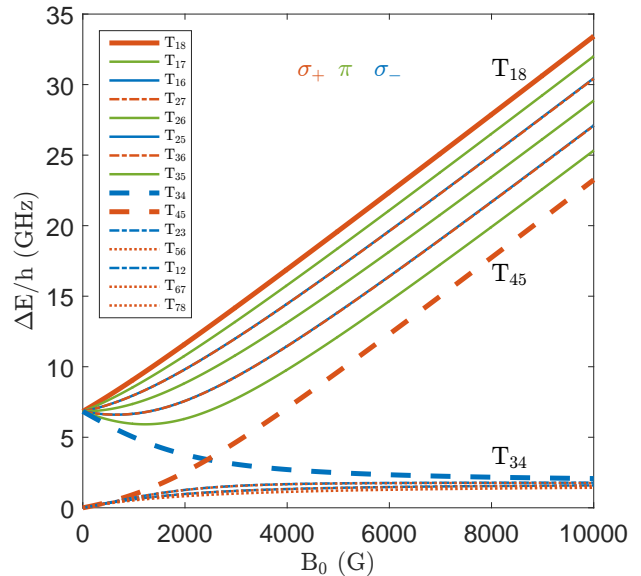


FIG. S1. Hyperfine transition frequencies as a function of applied dc magnetic field. The legend lists the transitions in order of decreasing frequency. The σ_+ transitions are shown in red, π transitions in green, and σ_- transitions are shown in blue. Dashed lines are used for clarity.

TABLE S1. Notation used for the ^{87}Rb $5S_{1/2}$ hyperfine levels. The levels $A_1 \rightarrow A_8$ are in order of increasing energy.

	Weak Field ($ F, m_F\rangle$)	General ($ m_I, m_J\rangle$)	Strong Field ($ m_I, m_J\rangle$)
A_1	$ 1, 1\rangle$	$a_1 3/2, -1/2\rangle + b_1 1/2, 1/2\rangle$	$ 3/2, -1/2\rangle$
A_2	$ 1, 0\rangle$	$a_2 1/2, -1/2\rangle + b_2 -1/2, 1/2\rangle$	$ 1/2, -1/2\rangle$
A_3	$ 1, -1\rangle$	$a_3 -1/2, -1/2\rangle + b_3 -3/2, 1/2\rangle$	$ -1/2, -1/2\rangle$
A_4	$ 2, -2\rangle$	$ -3/2, -1/2\rangle$	$ -3/2, -1/2\rangle$
A_5	$ 2, -1\rangle$	$a_5 -3/2, 1/2\rangle + b_5 -1/2, -1/2\rangle$	$ -3/2, 1/2\rangle$
A_6	$ 2, 0\rangle$	$a_6 -1/2, 1/2\rangle + b_6 1/2, -1/2\rangle$	$ -1/2, 1/2\rangle$
A_7	$ 2, 1\rangle$	$a_7 1/2, 1/2\rangle + b_7 3/2, -1/2\rangle$	$ 1/2, 1/2\rangle$
A_8	$ 2, 2\rangle$	$ 3/2, 1/2\rangle$	$ 3/2, 1/2\rangle$

$I = 3/2, J = 1/2$ for all of the levels, we abbreviate our notation to $|m_I, m_J\rangle$. The composition of each of the hyperfine levels in this basis is given Table S1. In general, each hyperfine level is a superposition of two $|m_I, m_J\rangle$ states, and the coefficients a and b can be determined by numerically diagonalising H . The two stretched states, $|F = 2, m_F = \pm 2\rangle \leftrightarrow |m_I = \pm 3/2, m_J = \pm 1/2\rangle$, are comprised of only a single $|m_I, m_J\rangle$ for all fields. In the absence of dc magnetic field, a and b are given by the Clebsch-Gordan coefficients, listed in Table S2. As the dc field strength increases, $a \rightarrow 1$ and $b \rightarrow 0$.

The strengths of the hyperfine transitions also change with the dc magnetic field, and are proportional to the $\langle f | J_\gamma | i \rangle$ matrix element, where $\gamma = -, \pi, +$ is the transition polarisation. We find that $\langle f | J_+ | i \rangle = a_i a_f$, $\langle f | J_- | i \rangle = b_i b_f$, and $\langle f | J_\pi | i \rangle = -\frac{1}{2} a_i b_f + \frac{1}{2} a_f b_i$, mean-

TABLE S2. Coefficients a and b in the $|m_I, m_J\rangle$ basis for the ^{87}Rb $5^2S_{1/2}$ hyperfine levels in the absence of external static magnetic field. The coefficients are the relevant Clebsch-Gordon coefficients for each state.

	$ F, m_F\rangle$	a	b
A ₁	$ 1, 1\rangle$	$\sqrt{3}/2$	$-1/2$
A ₂	$ 1, 0\rangle$	$1/\sqrt{2}$	$-1/\sqrt{2}$
A ₃	$ 1, -1\rangle$	$1/2$	$-\sqrt{3}/2$
A ₄	$ 2, -2\rangle$		
A ₅	$ 2, -1\rangle$	$1/2$	$\sqrt{3}/2$
A ₆	$ 2, 0\rangle$	$1/\sqrt{2}$	$1/\sqrt{2}$
A ₇	$ 2, 1\rangle$	$\sqrt{3}/2$	$1/2$
A ₈	$ 2, 2\rangle$		

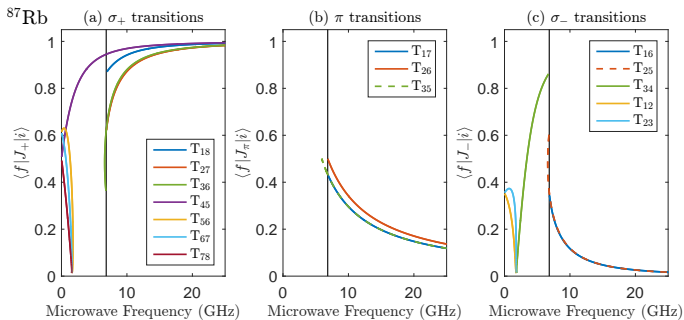


FIG. S2. Strengths of the σ_+ , π , and σ_- hyperfine transitions within the ^{87}Rb $5^2S_{1/2}$ ground state, as a function of the microwave transition frequency. The black vertical line is at 6.835 GHz. Data for ^{87}Rb was taken from Ref. [S3].

ing that as the magnetic field strength is increased, σ_+ transitions strengths approach unity, whilst σ_- transitions (rapidly) and π transitions (slowly) become weak. The σ_+ transition strengths between states with the same m_J value also go to zero at high dc fields. As a practical comparison, for $\langle f | J_\gamma | i \rangle = 1$, a $B_{\text{mw}} = 1 \mu\text{T}$ microwave field will drive $\Omega_R = 2\pi 28 \text{ kHz}$ Rabi oscillations, whilst for the same microwave field, $\langle f | J_\gamma | i \rangle = 0.1$ results in $\Omega_R = 2\pi 2.8 \text{ kHz}$.

A. Hyperfine Transitions for Microwave Sensing

The important considerations when choosing a hyperfine transition for microwave sensing are: the microwave frequency of interest, the hyperfine transition strength, the optical resolution of the hyperfine transition states (i.e. the degree to which absorption due to each state can be distinguished), the microwave polarisation of interest, and the dc magnetic field required to tune a hyperfine transition to frequency of interest. Supplementary figure S2 provides a useful analysis tool, showing the σ_+ , π , and σ_- transition strengths as a function of microwave transition frequency.

T₄₅ is the most versatile σ_+ transition, covering all

microwave frequencies above dc. Above 0.6 GHz, it is also the strongest σ_+ transition for a given microwave frequency. The optical resolution of the neighbouring A₄ and A₅ states can be poor, however, particularly at low B_{dc} (corresponding to low microwave frequencies). For microwave sensing of frequencies above 6.835 GHz, the best σ_+ transition is therefore generally T₁₈. The A₁ and A₈ levels are maximally spectrally resolved from one another, and optical transitions from these levels enjoy minimal background absorption due to ^{85}Rb . The T₁₈ transition is almost as strong as T₄₅ for a given microwave frequency, and requires much smaller B_{dc} to be tuned to a given frequency. For example, to achieve an 18 GHz microwave transition requires $B_{\text{dc}} = 0.44 \text{ T}$ on the T₁₈ transition, but $B_{\text{dc}} = 0.81 \text{ T}$ on the T₄₅ transition.

The selection of π microwave transition is less clear-cut. T₂₆ is the strongest π transition, but the difference with T₁₇ and T₃₅ is not dramatic. T₁₇ has the best optical resolution, due to the low ^{85}Rb absorption background for optical transitions from A₁ and the large spectral separation of the A₁ and A₇ levels. The T₃₅ transition is first-order insensitive to dc magnetic fields around $B_{\text{dc}} = 0.12 \text{ T}$, corresponding to a microwave frequency of 5.92 GHz, and is thus the optimal transition around this point. Supplementary figure S2 indicates that the π transitions can be used for sensing microwaves even above 20 GHz, with the T₂₆ transition strength dropping to $\langle 6 | J_\pi | 2 \rangle = 0.15$ at 22.8 GHz.

The σ_- transition strengths quickly drop away for microwave frequencies above 6.835 GHz, with the T₁₆ and T₂₅ transition strengths dropping to $\langle f | J_- | i \rangle = 0.15$ at 9.06 GHz. However, the T₃₄ transition can be used to detect microwaves below 6.835 GHz. The T₃₄ transition strength drops to $\langle 4 | J_- | 3 \rangle = 0.15$ at 2.17 GHz.

We can perform a similar analysis for other alkali species. The ranges of detectable frequencies for σ_+ , π , and σ_- polarised microwaves using ^{23}Na , ^{39}K , ^{85}Rb , and ^{133}Cs are summarised in Table S3. The frequency range was defined as that for which there is a transition with a strength above $\langle f | J_\gamma | i \rangle = 0.15$, neglecting transitions between states with the same m_J value. Strong σ_+ polarised transitions are available at all microwave frequencies and dc magnetic field strengths, and in order to compare the different alkali species, we took the maximum σ_+ frequency as the highest transition frequency available at our maximum solenoid field, $B_{\text{dc}} = 0.8 \text{ T}$. Vapor cells filled with multiple species can be used to span larger frequency ranges. For example, a natural Rb cell provides π transitions over the range 2.26–22.8 GHz.

IV. RECONSTRUCTION OF MICROWAVE FIELDS OF ARBITRARY FREQUENCY

In this section, we provide a framework for reconstructing microwave magnetic fields of arbitrary frequency, using ^{87}Rb atoms in an applied static magnetic field (\mathbf{B}_{dc})

TABLE S3. Summary of the transitions available in various alkali species for sensing the σ_+ , π , and σ_- components of a microwave field. I is the nuclear spin. The maximum σ_+ frequency is defined as the highest transition frequency available at our maximum solenoid field, $B_{dc} = 0.8$ T.

Isotope	Abundance	I	E_{hfs}/h (GHz)		Min. (GHz)	Max. (GHz)
^{23}Na	1	3/2	1.772	σ_+	0	23.8
				π	1.53	5.90
				σ_-	0.56	2.35
^{39}K	0.9326	3/2	0.462	σ_+	0	22.8
				π	0.40	1.54
				σ_-	0.15	0.61
^{85}Rb	0.7217	5/2	3.036	σ_+	0	25.0
				π	2.26	10.1
				σ_-	0.74	4.15
^{87}Rb	0.2783	3/2	6.835	σ_+	0	27.9
				π	5.92	22.8
				σ_-	2.17	9.06
^{133}Cs	1	7/2	9.193	σ_+	0	30.8
				π	6.08	30.6
				σ_-	1.62	12.7

of any strength. This builds on the framework given for the weak dc field regime in Ref. [S4]. The framework is not restricted to ^{87}Rb , and is valid for microwave transitions in a general system.

In the fixed lab-frame cartesian coordinate system, (x, y, z) , a microwave magnetic field is defined by

$$\mathbf{B} \equiv \begin{pmatrix} B_x e^{-i\phi_x} \\ B_y e^{-i\phi_y} \\ B_z e^{-i\phi_z} \end{pmatrix}.$$

In order to reconstruct this field, we need to find these six real values, $B_{x,y,z}, \phi_{x,y,z} \in \mathfrak{R}_{\geq 0}$, which are each an implicit function of spatial position. We do this by measuring Rabi oscillations driven by the microwave field on atomic hyperfine transitions. The quantisation axis of our measurements is defined by the applied dc magnetic field, \mathbf{B}_{dc} . Following Ref. [S4], we define a primed cartesian coordinate system, (x', y', z') , with the z' axis pointing along the direction of \mathbf{B}_{dc} . The π and σ_{\pm} components of the microwave field in the primed frame are

$$B_- e^{-i\phi_-} \equiv \frac{1}{2} [B_{x'} e^{-i\phi_{x'}} + iB_{y'} e^{-i\phi_{y'}}], \quad (\text{S3})$$

$$B_{\pi} e^{-i\phi_{\pi}} \equiv B_{z'} e^{-i\phi_{z'}}, \quad (\text{S4})$$

$$B_+ e^{-i\phi_+} \equiv \frac{1}{2} [B_{x'} e^{-i\phi_{x'}} - iB_{y'} e^{-i\phi_{y'}}], \quad (\text{S5})$$

with $B_{-, \pi, +}, \phi_{-, \pi, +} \in \mathfrak{R}_{\geq 0}$. For transitions from an initial state $|1\rangle$ to a final state $|2\rangle$, the Rabi frequencies

are

$$\Omega_- \equiv \frac{2\mu_B}{\hbar} \langle 2 | J_- | 1 \rangle B_- e^{-i\phi_-}, \quad (\text{S6})$$

$$\Omega_{\pi} \equiv \frac{2\mu_B}{\hbar} \langle 2 | J_z | 1 \rangle B_{\pi} e^{-i\phi_{\pi}}, \quad (\text{S7})$$

$$\Omega_+ \equiv \frac{2\mu_B}{\hbar} \langle 2 | J_+ | 1 \rangle B_+ e^{-i\phi_+}, \quad (\text{S8})$$

Where $J_z, J_+ = J_x + iJ_y$, and $J_- = J_x - iJ_y$ are the spin z , raising, and lowering operators, respectively.

Note that in the definitions of B_- and B_+ , a factor of $1/\sqrt{2}$ instead of $1/2$ can also be found in some of the literature. This goes along with a change in the definitions of J_+ and J_- , which then read $J_{\pm} = \frac{1}{\sqrt{2}}(J_x \pm iJ_y)$. If this alternative definition is used, the coefficients α_+ and α_- are larger by a factor of $\sqrt{2}$.

A. Microwave Amplitude

From Eq. (S7), it is straightforward to determine the amplitudes of the microwave magnetic field ($B_{x,y,z}$) when strong π transitions are present. The matrix element $\langle f | J_z | i \rangle$ can be calculated numerically for a any static magnetic field, and so we can obtain the amplitudes along each axis by measuring $|\Omega_{\pi}|$ with the quantisation axis along x, y and z respectively. The π (and σ_-) transitions become weak in strong dc fields, however, and in the general case, we need to determine the microwave field amplitudes using only σ_+ transitions.

In the following discussion, the superscript index represents the quantisation axis in the lab frame, i.e. the direction of the applied static magnetic field. Thus for example, Ω_+^{+y} (B_+^{+y}) means Ω_+ (B_+) for \mathbf{B}_{dc} pointing

along the y axis in the positive direction, whilst Ω_+^{-y} (B_+^{-y}) is for \mathbf{B}_{dc} pointing along the y axis in the negative direction.

We begin by finding the sum of B_-^2 and B_+^2 . From Eq. (S8) we see that for σ_+ transitions, we only obtain B_+ . However, for measurements along a given axis, B_+ measured antiparallel to that axis is equivalent to B_- measured parallel to the axis. That is, $B_- = B_+$. By measuring $|\Omega_+|$ with the static field both parallel and antiparallel to our axis of measurement, we can thus obtain both B_+ and B_- . This gives us

$$B_-^2 + B_+^2 = \frac{\hbar^2}{4\mu_B^2} \left[\frac{|\Omega_+^-|^2}{|\langle f | J_+ | i \rangle|^2} + \frac{|\Omega_+^+|^2}{|\langle f | J_+ | i \rangle|^2} \right]. \quad (\text{S9})$$

We can also find the $B_-^2 + B_+^2$ sum using Eqs. (S3) and (S5). Equating this with Eq. (S9) gives

$$\frac{1}{2}(B_{x'}^2 + B_{y'}^2) = \frac{\hbar^2}{4\mu_B^2} \left[\frac{|\Omega_+^-|^2}{|\langle f | J_+ | i \rangle|^2} + \frac{|\Omega_+^+|^2}{|\langle f | J_+ | i \rangle|^2} \right]. \quad (\text{S10})$$

Defining

$$K_+ \equiv \frac{|\Omega_+^-|^2}{|\langle f | J_+ | i \rangle|^2} + \frac{|\Omega_+^+|^2}{|\langle f | J_+ | i \rangle|^2}, \quad (\text{S11})$$

we can write

$$B_{x'}^2 + B_{y'}^2 = \frac{\hbar^2}{2\mu_B^2} K_+. \quad (\text{S12})$$

Next, we apply this formula with the quantisation axis defined along each of the x , y and z axes. Starting with \mathbf{B}_{dc} (and thus z') along the x axis, we transform from the primed coordinate system back into the unprimed lab frame, according to the following coordinate transformation:

$$\begin{aligned} x' &= -z, \\ y' &= y, \\ z' &= x. \end{aligned} \quad (\text{S13})$$

This transforms the microwave magnetic field phasor to

$$\mathbf{B} \equiv \begin{pmatrix} B_{x'} e^{-i\phi_{x'}} \\ B_{y'} e^{-i\phi_{y'}} \\ B_{z'} e^{-i\phi_{z'}} \end{pmatrix} = \begin{pmatrix} -B_z e^{-i\phi_z} \\ B_y e^{-i\phi_y} \\ B_x e^{-i\phi_x} \end{pmatrix},$$

with

$$\begin{aligned} B_{x'} &= B_z & \phi_{x'} &= \phi_z + \pi, \\ B_{y'} &= B_y & \phi_{y'} &= \phi_y, \\ B_{z'} &= B_x & \phi_{z'} &= \phi_x. \end{aligned} \quad (\text{S14})$$

Applying this coordinate transformation to Eq. (S12) then gives us

$$B_z^2 + B_y^2 = \frac{\hbar^2}{4\mu_B^2} K_+, \quad (\text{S15})$$

with K_+ defined in Eq. (S21). We can follow a similar process for \mathbf{B}_{dc} along the y and z axes to get

$$B_z^2 + B_x^2 = \frac{\hbar^2}{4\mu_B^2} K_+, \quad (\text{S16})$$

$$B_x^2 + B_y^2 = \frac{\hbar^2}{4\mu_B^2} K_+. \quad (\text{S17})$$

Solving these equations simultaneously gives the magnitude of the magnetic field along the (lab frame) x , y , and z directions,

$$B_x^2 = \frac{\hbar^2}{8\mu_B^2} \left[-K_+^x + K_+^y + K_+^z \right], \quad (\text{S18})$$

$$B_y^2 = \frac{\hbar^2}{8\mu_B^2} \left[K_+^x - K_+^y + K_+^z \right], \quad (\text{S19})$$

$$B_z^2 = \frac{\hbar^2}{8\mu_B^2} \left[K_+^x + K_+^y - K_+^z \right], \quad (\text{S20})$$

where K_+^γ is defined as

$$K_+^\gamma \equiv \frac{|\Omega_+^{-\gamma}|^2}{|\langle f | J_+ | i \rangle|^2} + \frac{|\Omega_+^{+\gamma}|^2}{|\langle f | J_+ | i \rangle|^2}. \quad (\text{S21})$$

$|\Omega_+^{-\gamma}|$ and $|\Omega_+^{+\gamma}|$ are experimentally determined quantities. The matrix element $\langle f | J_+ | i \rangle$ can be calculated numerically for a general applied static magnetic field, \mathbf{B}_{dc} .

B. Microwave Phase

To reconstruct the field phases, ϕ_x , ϕ_y and ϕ_z , we begin with the difference of B_-^2 and B_+^2 . Again, this can be found using Eq. (S8), measuring $|\Omega_+|$ with the static field both parallel and antiparallel to our axis of measurement, and also using Eqs. (S3) and (S5):

$$\begin{aligned} B_-^2 - B_+^2 &= \frac{\hbar^2}{4\mu_B^2} \left[\frac{|\Omega_+^-|^2}{|\langle f | J_+ | i \rangle|^2} - \frac{|\Omega_+^+|^2}{|\langle f | J_+ | i \rangle|^2} \right] \\ &= B_{x'} B_{y'} \sin(\phi_{y'} - \phi_{x'}). \end{aligned} \quad (\text{S22})$$

This time we define

$$K_- \equiv \frac{|\Omega_+^-|^2}{|\langle f | J_+ | i \rangle|^2} - \frac{|\Omega_+^+|^2}{|\langle f | J_+ | i \rangle|^2}, \quad (\text{S23})$$

and so we have

$$\sin(\phi_{y'} - \phi_{x'}) = \frac{\hbar^2}{4\mu_B^2 B_{x'} B_{y'}} K_-. \quad (\text{S24})$$

We measure $|\Omega_+|^2$ parallel and antiparallel to the x , y , and z axes, and use Eq. (S24) with the same coordinate

transformations as in Section IV A. Inserting the field magnitudes obtained with Eqs. (S18-S20), we get

$$\sin(\phi_z - \phi_y) = \quad (S25)$$

$$2 \left[(K_+^x - K_+^y + K_+^z)(K_+^x + K_+^y - K_+^z) \right]^{-1/2} K_-^x,$$

$$\sin(\phi_x - \phi_z) = \quad (S26)$$

$$2 \left[(-K_+^x + K_+^y + K_+^z)(K_+^x + K_+^y - K_+^z) \right]^{-1/2} K_-^y,$$

$$\sin(\phi_y - \phi_x) = \quad (S27)$$

$$2 \left[(-K_+^x + K_+^y + K_+^z)(K_+^x - K_+^y + K_+^z) \right]^{-1/2} K_-^z,$$

with K_+^γ as defined in equation S21 and K_-^γ defined as K_- for a static magnetic field along the direction γ :

$$K_-^\gamma \equiv \frac{|\Omega_+^{-\gamma}|^2}{|\langle f | J_+ | i \rangle|^2} - \frac{|\Omega_+^{+\gamma}|^2}{|\langle f | J_+ | i \rangle|^2}. \quad (S28)$$

$|\Omega_+^{-\gamma}|$ and $|\Omega_+^{+\gamma}|$ are experimentally determined quantities. The matrix elements $\langle f | J_- | i \rangle$ and $\langle f | J_+ | i \rangle$ can be calculated numerically for a general applied static magnetic field, \mathbf{B}_{dc} . From Eqs. (S25-S27), we can obtain the relative phases of the B_{mw} components.

[S1] S. Kadlecěk, T. Walker, D. K. Walter, C. Erickson, and W. Happer, *Physical Review A* **63**, 052717 (2001).

[S2] A. Horsley, G.-X. Du, and P. Treutlein, *New J. Phys.* **17**, 112002 (2015).

[S3] D. A. Steck, “Rubidium 87 D Line Data,” available online at <http://steck.us/alkalidata> (revision 2.1.4, 23 December 2010).

[S4] P. Böhi, M. F. Riedel, T. W. Hänsch, and P. Treutlein, *Appl. Phys. Lett.* **97**, 051101 (2010).